WILEY | Hindawi

Research Article

Characteristic-Based Fluid Flow Modeling between Two Eccentric Cylinders in Laminar and Turbulent Regimes

Tohid Adibi,[1] **Seyed Esmail Razavi,**[2] **Shams Forruque Ahmed** ⓘ **,**[3] **Aria Amrikachi,**[4] **and Suvash C. Saha**[5]

[1]School of Mechanical Engineering, University of Bonab, Bonab, Iran
[2]School of Mechanical Engineering, University of Tabriz, Tabriz, Iran
[3]Science and Math Program, Asian University for Women, Chattogram 4000, Bangladesh
[4]Department of Mechanical Engineering, Shahid Beheshti University, Tehran, Iran
[5]School of Mechanical and Mechatronic Engineering, University of Technology Sydney, Sydney, Australia

Correspondence should be addressed to Shams Forruque Ahmed; shams.ahmed@auw.edu.bd

Determining the flow between eccentric cylinders is crucial in a wide range of industries. The governing equations for the flow between eccentric cylinders cannot be solved analytically. Therefore, three-dimensional incompressible viscous fluid flow between eccentric and concentric cylinders has numerically been simulated in this paper to investigate them using a characteristic-based approach. The first-order characteristic-based scheme is used to calculate convective terms, whereas the second-order averaging technique is used to calculate viscous fluxes. The Taylor number, eccentricity distance, Reynolds number, and radius ratio are considered the controlling parameters of fluid flow between the cylinders. The influence of flow between cylinders on flow patterns is presented in terms of velocity, pressure, and flow contours. It is found that at a constant Taylor number, the asymmetric centrifugal forces produce the Taylor vortices on the right of the internal rotating cylinder as the eccentric distance increases. When the eccentric distance increases, the magnitude of shear stress and its fluctuation on the cylinder wall, as well as the pressure on the cylinder wall, rise. The numerical results obtained were validated by comparing them to previously published experimental results, which showed a high level of agreement.

1. Introduction

Researchers have conducted several numerical studies during the last few decades. Thermo-flows, or flows involving heat transfer, are the most challenging issues [1] that can be solved numerically. Quiet flows are most frequently used in journal bearings. Oil or fluid withstands the proper pressure difference to sustain radial loads on the axis caused by eccentric cylinders and axis rotation due to fluid viscosity sucking into wedge-shaped spaces, hence avoiding axial wear. Internal cylindrical rotation causes the fluid to rotate in the space [2], and in some regimes, the rotational speed causes vortex appearance in the flow. Across a cylinder, a three-dimensional incompressible numerical study on thermo-flow was conducted by Reddy

et al. [3]. The flow was found turbulent, and the $k - \omega$ method was used for simulating the turbulence. The simulations were run for a wide range of Reynolds (Re) numbers, and the mean Nuselt number and drag force in various scenarios were calculated and compared.

Kim and Hwang [4] numerically examined the flow between two cylinders where the internal cylinder was rotating. They measured the effects of rotational speed, the flow rates, and the working fluids on the pressureless and skin friction coefficients. A strong correlation was found between skin friction coefficients, Rossby numbers, and Reynolds numbers in the laminar regimes. It was also demonstrated that, when the Rossby number increases as the rotational speed increases, the critical Reynolds number lowers as

expected. Several kinds of research on hydrodynamic lubrication examined the flow around the cylinder. For instance, Ma et al. [5] studied the abnormal behavior of hydrodynamic lubrication caused by wall sliding in journal bearings using the Reynolds equation with the finite element method. The results illustrated that if the lubricated surfaces are designed as homogeneous slip surfaces, sliding on the wall reduces the oil film's load support. If there is a slip on the wall at lubricating surfaces, the hydrodynamic impact of the bearing is diminished, and the bearing is unable to withstand loads. To prevent slipping on the wall, the shear stress limit on the bearing surfaces must be greater than the values on the axis surface.

The classical hydrodynamic lubrication theory assumes that the oil flow regime is laminar and that the inertia fluid forces of the fluid film are negligible [6]. For large bearings using low-viscosity lubricants or for high speed, inertial forces can be significant because in such cases, nonlaminar flow occurs. To investigate lubrication at high Reynolds numbers, Frêne et al. [7] performed a combined analysis of thin-film and Navier-Stokes equations. This study provided an overview of nonlaminar lubrication. Various flow regimes occurring in bearings and seals were shown, and theories for obtaining flow characteristics were presented in the nonlaminar state. The effects of inertial forces on laminar and turbulent currents were investigated, and the results of solving the complete Navier-Stokes equations were presented and compared to the classical lubrication theory. Singh et al. [8] performed a theoretical steady-state thermo-hydrodynamic analysis of axial groove journal bearings with oil supplied at constant pressure. The thermo-hydrodynamic study required simultaneous solutions of the Reynolds equation, energy equation, and heat transfer equations in bush and shaft. It was revealed that the oil film temperature is increased due to the thermal friction, and consequently, the fluid viscosity increases and reduces bearing load capacity. The increased shaft speed causes an increase in load-bearing capacity, bush temperature, flow rate, and friction variable. However, solving the problem due to numerical instability is complicated when the bearing is operating at high eccentricity ratios.

Bhatti et al. [9] conducted a semianalytical study in a fluid flow exposed to an electromagnetic field where the Nusselt numbers were obtained for different parameters. A differential transform method was used to obtain the numerical results of nonlinear coupled differential equations. The comparison was done using a shooting scheme for the Nusselt number. The proposed scheme was found stable to solve the nonlinear differential equations. Shahid et al. [10] worked on a nanofluid flow over a porous wall with a sinusoidal solid boundary. The flow was exposed to an electromagnetic field, and governing equations were obtained by considering non-Newtonian fluid. A similarity solution was used to transform the governing equations into ordinary differential equations. The obtained equations were solved by implementing the spectral local linearization technique numerical method. Bhatti et al. [11] also performed a numerical analysis on a fluid flow with nanoparticles. The flow was limited by two circular parallel solid boundaries

with an angular velocity. The nanofluid flow was subjected to an electromagnetic field, and the obtained outcome can be used for thermal energy storage systems.

Roy and Laha [12] theorized the dynamic and steady-state characteristics, including the eddy instability of the oil in the bearing with the axial groove at different positions, while the oil was fed at constant pressure. The Reynolds equation was numerically solved using the finite difference method and proper boundary conditions. The results showed that when the groove is at 12°, both the load capacity and the currents are at their maximum and begin to diminish at subsequent positions. In high eccentricity and velocity cases, the stability for lower angles and groove lengths got improved. The stiffness and damping coefficient values were higher for grooves with small angles and shorter lengths. Kumar et al. [13] studied the effect of a magnetic field on the flow between two concentric rotating cylinders. The equations governing the Jeffrey fluid were employed in the cylindrical coordinates. Squadron fixed point theory was used for the analysis of momentum equations. The studies discussed above mainly investigated the flow patterns in different regimes. However, all of the key parameters that affect the performance of the cylinders such as the Taylor number, Reynolds number, eccentricity ratio, and fluid viscosity were not considered in those studies, and thus, the actual performance of the cylinders did not reflect. Therefore, the present study assesses the 3D (three-dimensional) flow pattern to measure the cylinder performance in two flow regimes by considering these as the controlling parameters.

2. Governing Equations

The governing equations (continuity, momentum in three dimensions, and energy equation) for the incompressible unsteady flow in the cylindrical coordinates are [14]

$$
\begin{aligned}
&\frac{1}{r}\frac{\partial}{\partial r}(ru_r) + \frac{1}{r}\frac{\partial u_\varnothing}{\partial \varnothing} + \frac{\partial u_z}{\partial z} \\
&= 0 \; \frac{\partial u_r}{\partial t} + \frac{1}{r}\frac{\partial}{\partial r}(ru_r u_r) + \frac{1}{r}\frac{\partial}{\partial \varnothing}(ru_r u_\varnothing) - \frac{u_\varnothing^2}{r} + \frac{\partial}{\partial z}(u_z u_r) \\
&= -\frac{1}{\rho r}\frac{\partial p}{\partial r} + \vartheta\left[\frac{1}{r}\frac{\partial}{\partial r}\left(r\frac{\partial u_r}{\partial r}\right) + \frac{1}{r^2}\frac{\partial^2 u_r}{\partial \varnothing^2} - \frac{u_r}{r^2} - \frac{2}{r^2}\frac{\partial u_\varnothing}{\partial \varnothing} + \frac{\partial^2 u_r}{\partial z^2}\right] \\
&\quad + g\beta(T - T_0)\sin(\varnothing)\;\frac{\partial u_\varnothing}{\partial t} + \frac{1}{r}\frac{\partial}{\partial r}(ru_r u_\varnothing) + \frac{1}{r}\frac{\partial}{\partial \varnothing}(u_\varnothing^2) \\
&\quad + \frac{u_r u_\varnothing}{r} + \frac{\partial}{\partial z}(u_z u_\varnothing) = -\frac{1}{\rho r}\frac{\partial p}{\partial \varnothing} \\
&\quad + \vartheta\left[\frac{1}{r}\frac{\partial}{\partial r}\left(r\frac{\partial u_\varnothing}{\partial r}\right) + \frac{1}{r^2}\frac{\partial^2 u_\varnothing}{\partial \varnothing^2} - \frac{u_\varnothing}{r^2} + \frac{2}{r^2}\frac{\partial u_r}{\partial \varnothing} + \frac{\partial^2 u_\varnothing}{\partial z^2}\right] \\
&\quad + g\beta(T - T_0)\cos(\varnothing) - \frac{\partial u_z}{\partial t} + \frac{1}{r}\frac{\partial}{\partial r}(ru_r u_z) \\
&\quad + \frac{1}{r}\frac{\partial}{\partial \varnothing}(u_z u_\varnothing) + \frac{\partial}{\partial z}(u_z^2) = -\frac{1}{\rho}\frac{\partial p}{\partial z} \\
&\quad + \vartheta\left[\frac{1}{r}\frac{\partial}{\partial r}\left(r\frac{\partial u_z}{\partial r}\right) + \frac{1}{r^2}\frac{\partial^2 u_z}{\partial \varnothing^2} + \frac{\partial^2 u_z}{\partial z^2}\right]\frac{\partial T}{\partial t} + \frac{1}{r}\frac{\partial}{\partial r}(ru_r T) \\
&\quad + \frac{1}{r}\frac{\partial}{\partial \varnothing}(Tu_\varnothing) + \frac{\partial}{\partial z}(u_z T) = \alpha\left[\frac{1}{r}\frac{\partial}{\partial r}\left(r\frac{\partial T}{\partial t}\right) + \frac{1}{r^2}\frac{\partial^2 T}{\partial \varnothing^2} + \frac{\partial^2 T}{\partial z^2}\right],
\end{aligned}
$$

$$(1)$$

where u_r, u_Φ, u_z represents the fluid velocities, T denotes the temperature, P signifies the pressure, t is the time, T_0 is the reference temperature, and g and β are the gravitational and thermal compressibility coefficient, respectively. The r, z, and $\varnothing$ represent the directions in cylindrical coordinates. A term $g\beta(T - T_0)$ was added to the governing equation (1) that decomposes in two directions r, Φ. The Boussinesq approximation was used to consider the free convection effect. The density change was thus assumed to be negligible, and the flow was considered incompressible. The governing equation was used for laminar flow. Therefore, the two-equation turbulent scheme, k-ε turbulence model, was used to assess the turbulent flow behavior. The governing equations for the k-ε turbulence model are presented below [14].

$$\frac{\partial(\rho k)}{\partial t} + \frac{\partial(\rho k u_j)}{\partial x_j} = \frac{\partial}{\partial x_j}\left[\frac{\mu_t}{\sigma_k}\frac{\partial}{\partial x_j}\right] + 2\mu_t E_{ij}E_{ij} - \rho\varepsilon,$$

$$\frac{\partial(\rho\varepsilon)}{\partial t} + \frac{\partial(\rho\varepsilon u_j)}{\partial x_j} = \frac{\partial}{\partial x_j}\left[\frac{\mu_t}{\sigma_\varepsilon}\frac{\partial}{\partial x_j}\right] + 2C^{\varepsilon 1}\frac{\varepsilon}{k}\mu_t E_{ij}E_{ij} - \rho\varepsilon C^{\varepsilon 2}\frac{\varepsilon}{k},$$

$$\mu_t = \rho C^\mu \frac{k^2}{\varepsilon}, C^\mu = 0.09, \sigma_\varepsilon = 1.3, C^{\varepsilon 1} = 1.44, C^{\varepsilon 2} = 1.92.$$

$$(2)$$

In the system of equation (2), the first equation represents turbulent kinetic energy and the second one shows the dissipation equation.

3. Numerical Approaches

The fluid flow modeling analysis was performed by a code written in FORTRAN, and the effect of the parameters on cylinder performance was investigated in both laminar and turbulent regimes. The k-ε turbulence model was used for turbulent flow. The finite volume method was applied for numerical solutions. The numerical results obtained were validated with the experimental data and the results of other models. The three-dimensional characteristic-based scheme was utilized for convective fluxes whereas the second-order averaging method was used to calculate viscous fluxes. Time marching was obtained by using the fifth-order Runge-Kutta method. The inner cylinder was considered a rotary cylinder, while the outer cylinder was regarded as fixed. The rotational Reynolds number was calculated from the following equation:

$$\text{Re}_{\varnothing m} = \frac{\rho\Omega a(b - a)}{\mu},$$

$$(3)$$

where Re is the Reynolds number, a and b are the diameter of the cylinders, σ is the angular velocity, and μ is the viscosity of the fluid.

4. Results and Discussion

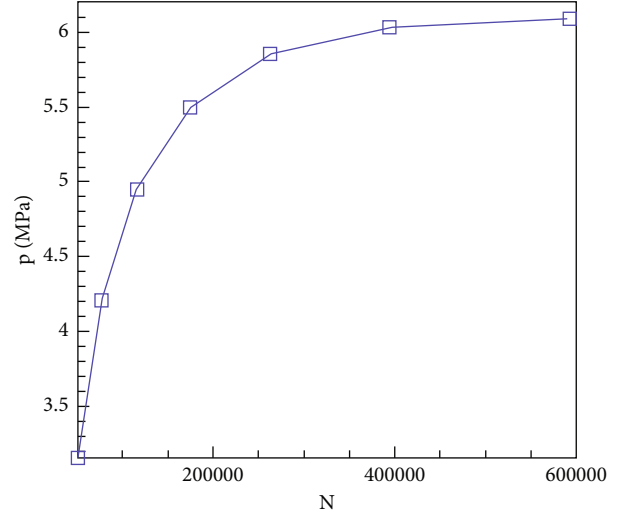The problem was simulated for various grids to test the grid independence on the simulations. The pressure on the cylin-

FIGURE 1: Pressure on the cylinder for Re = 48000, $\kappa = 0.2$, and $\varepsilon = 0.9$ at $\theta = 30°$ at different cell numbers.

der for different mesh sizes is shown in Figure 1. In this figure, the diameter respect and the eccentricity are defined as κ and ε, respectively, and θ is the angle on the cylinder. To obtain grid independence, simulations with different grids at $\kappa = 0.2$, $\varepsilon = 0.9$, and Re = 48000 were performed. The pressure distribution across the cylinder was obtained at different angles through the simulation. The pressure obtained at $\theta = 30°$ was compared in different grids. The grid independence was achieved when this pressure was nearly constant.

The results for a grid with 591856 elements differed little from those for a grid with 394571 elements. Therefore, the grid having 591865 elements was chosen for the simulations. Other simulations with different κ, ε, and Re were performed, and the results have been shown in the following figures. The grids in both two and three dimensions are presented in Figure 2. The geometric parameter and boundary conditions are defined in this figure. The inner cylinder is rotating with constant angular velocity, and the outer cylinder is fixed. No-slip condition is considered in solid boundaries.

The numerical results were compared with the experimental observation obtained by Escudier et al. [15] to validate them. The velocity profiles obtained at three different cross sections were compared and are presented in Figure 3. This section investigates the effect of eccentricity on current properties. Several numerical tests were conducted to ensure the configuration and correctness of Taylor vortices. The flow is simulated with a radius of 0.2 and a Taylor number of 50 with the inner cylinder rotated counterclockwise. Figure 4 shows the streamlines of Taylor vortices with this radius ratio and Taylor number at the exit in different eccentricities.

As illustrated in Figure 4, the vortices behave differently under various conditions. Asymmetric centrifugal effects increase as eccentricity rises, resulting in Taylor vortex formation on the right side of the inner cylinder. In the small inner cylinder with low eccentricity, no Taylor vortices are seen. The magnitude of velocity is also low in Taylor
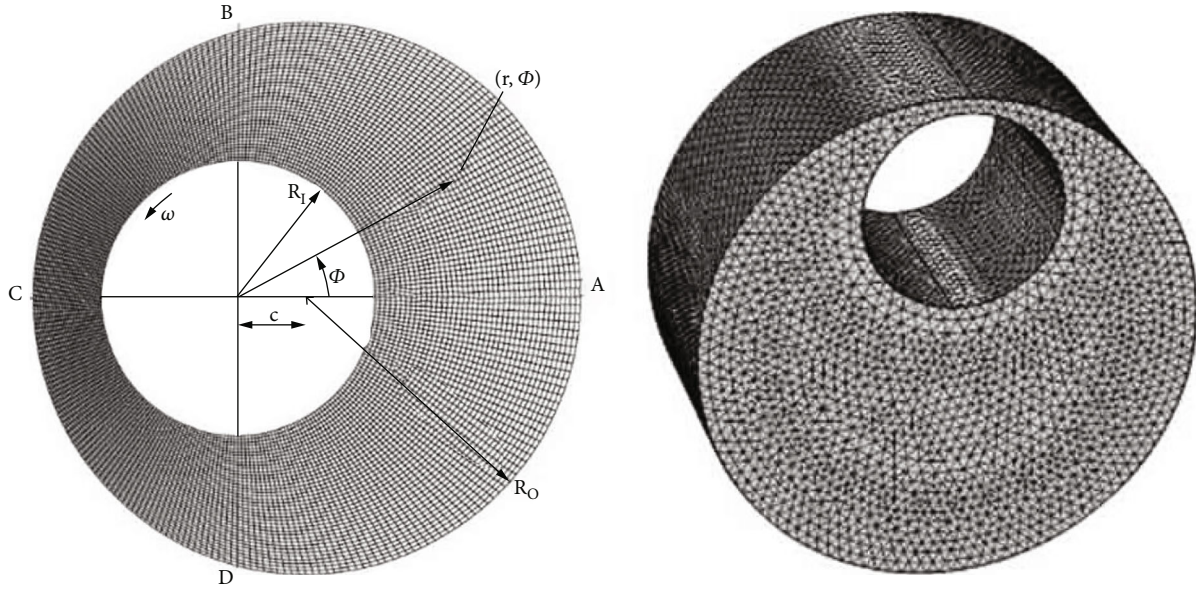
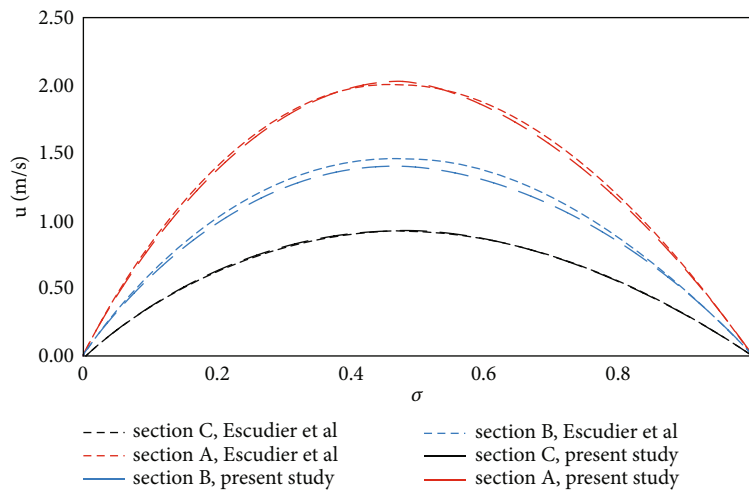FIGURE 2: Grids in two and three dimensions with the geometric parameters.

FIGURE 3: Comparison of velocity distribution in different sections of nested cylinders with the results of Escudier et al. [15].

vortices. However, there is a large Taylor vortex in medium and high eccentricity. This vortex becomes thinner when the radius of the inner cylinder is increased. The Taylor vortices are generated because of the reverse flow that occurs in the flow field. Centrifugal acceleration causes the fluid to flow in a radial direction, resulting in the formation of Taylor vortices and a low-pressure zone in that region of the flow. The formation of Taylor vortices changes the pressure field and thus modifies the bearing forces.

At a radius ratio of 0.2, Figure 5 depicts the shear stress distribution around the revolving inner cylinder as eccentricity increases. The shear stress diagram surrounding the cylinder demonstrates that when the eccentricity of the two cylinders and the asymmetry of the velocity distribution increase, the velocity gradients and shear stress rise as well. It is seen that most shear stress occurs at an angle of 180

degrees. This is due to the high-velocity gradients in the region. The proximity of two solid walls in the area mainly increases this velocity gradient.

Simulations were repeated for the radius ratio of 0.8 to survey the flow characteristics. The pressure contours for different eccentricities and the pressure distribution on the cylinder are shown in Figures 6 and 7, respectively. As seen in the figures, the isobar lines shift and the location of the maximum and minimum pressure also changes; therefore, the location of these pressures also fluctuates as a result of the eccentricity change. Maximum and minimum pressure approaches 180° as eccentricity increases. Proximity to the solid wall is the main reason behind this.

The pressure distribution diagram for different Taylor numbers around the cylinder is illustrated in Figure 8. The figure shows that as the Taylor number increases, the

$$\varepsilon = 0.9 \qquad \varepsilon = 0.6 \qquad \varepsilon = 0.3$$
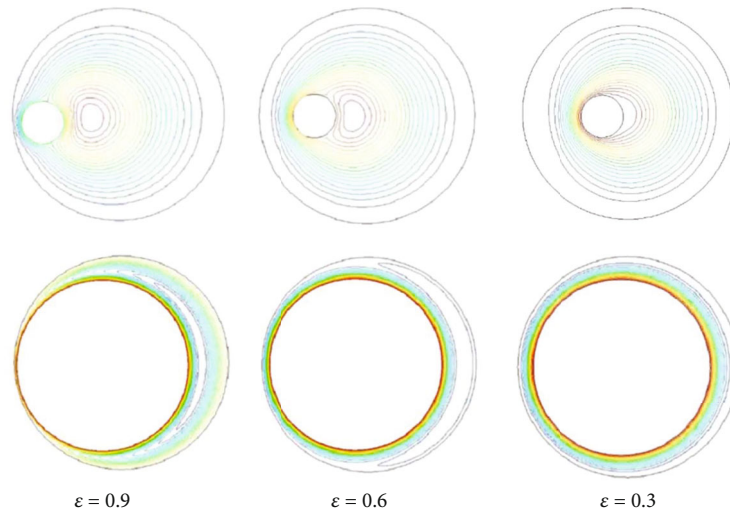
FIGURE 4: Streamlines showing Taylor vortices with a radius ratio of 0.2 and Taylor number of 50 at the exit in different eccentricities.
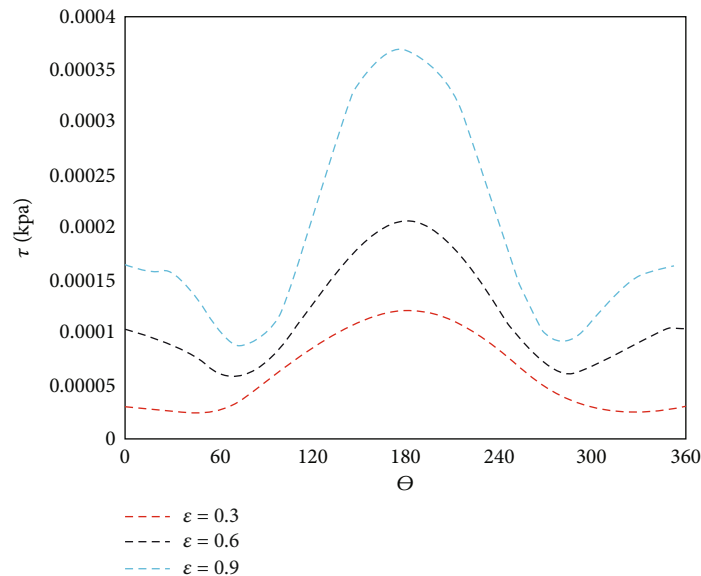

FIGURE 5: Diagram of shear stress distribution around the cylinder at different ε at $\kappa = 0.2$ and Ta = 50.

pressure on the inner cylinder increases as well. The pressure variations on the inner cylinder become more complex as the Taylor number increases, and the pressure diagram has different local maximum and minimum. The absolute maximum and minimum occur at around an angle of 180 degrees. As the Taylor number increases, the amount of pressure at different angles increases with approximately the same coefficient.

According to the pressure distribution diagrams for different Taylor numbers, it is observed that in the lower part of the bearing, the pressure is greater than that of the wider bearing part, due to the pumping of current by the viscous forces into the wedge-shaped space. This pressure difference generates a perpendicular radial force and can endure radial forces because of the axial loading. The magnitude of this pressure difference on the sides of the axis and therefore the bearing force of the bearing depends on the current Taylor number. Furthermore, vortices do not arise in general for flows between two rotating cylinders when the impurity is too small such as in journal bearings. This is because the outer cylinder wall interferes with the flow, preventing the formation of a separate fluid flow region. The variations in the velocity along the y-axis for different Reynolds numbers are shown in Figure 9.

As seen in Figure 9, the velocity increases when the Reynolds number increases. Additionally, given the nonslip fluid condition and the stationary state of both cylinders, the velocities on both sides are zero. The main reason for these zero velocities is that both cylinders are stationary and there is an axial pressure gradient. The boundary layer formed on both cylinders can be noticed depending on the velocity profiles. Outside the boundary layer, the velocity is
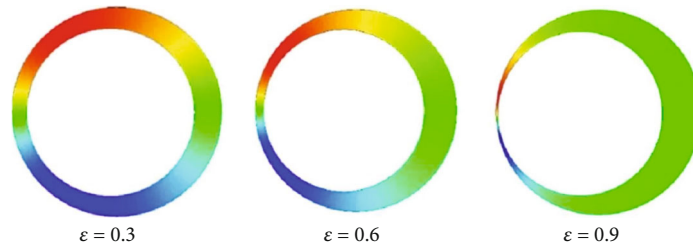
$\varepsilon = 0.3$ $\varepsilon = 0.6$ $\varepsilon = 0.9$

FIGURE 6: Pressure contours for $\kappa = 0.8$, Ta = 50, and eccentricities.

- - - $\varepsilon = 0.3$
- - - $\varepsilon = 0.6$
- - - $\varepsilon = 0.9$
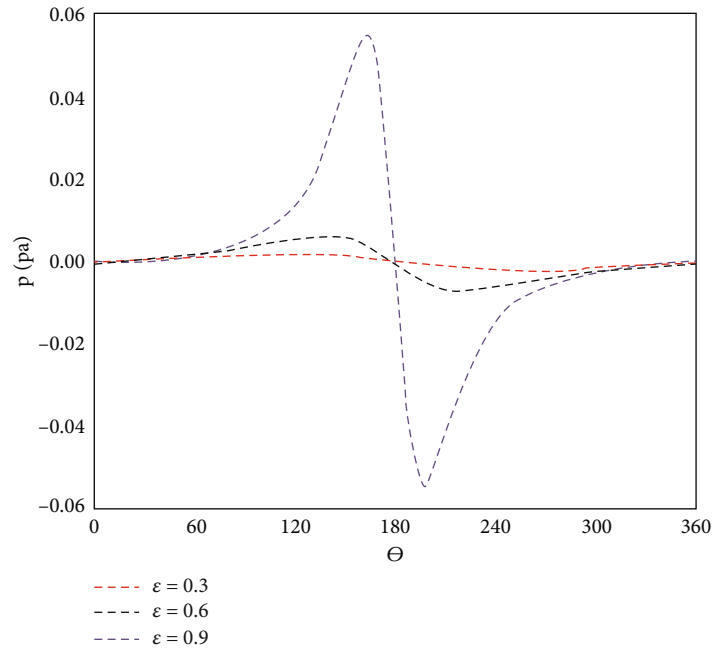
FIGURE 7: Pressure changes around the cylinder at different ε and $\kappa = 0.8$ and Ta = 50.

...... Ta = 50   - - - Ta = 5000
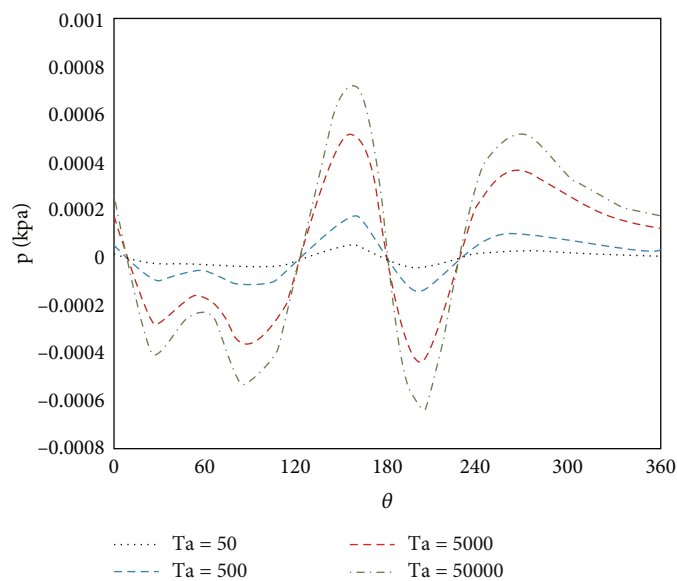- - - Ta = 500   -·-· Ta = 50000

FIGURE 8: Pressure distribution for different Taylor numbers around cylinders at $\kappa = 0.2$ and $\varepsilon = 0.9$.
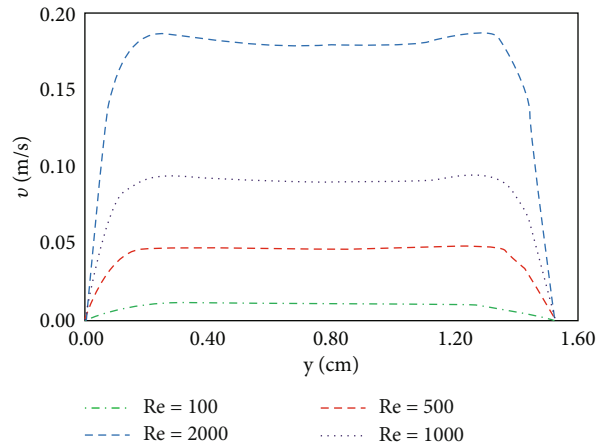
Figure 9: The velocity distribution along the y-axis for different Reynolds numbers at $\kappa = 0.2$ and $\varepsilon = 0.9$.
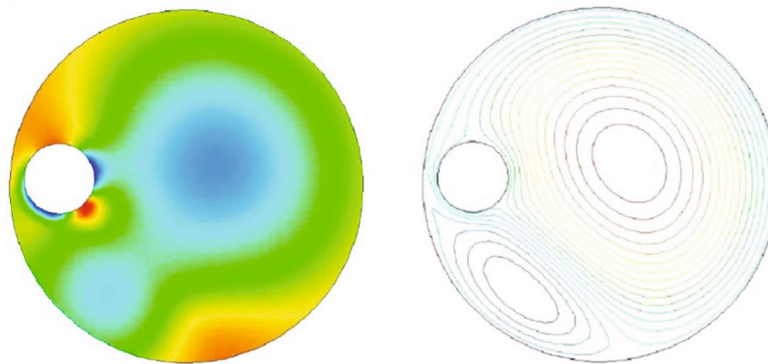

Figure 10: The velocity distribution along the y-axis for different Reynolds numbers at $\kappa = 0.2$ and $\varepsilon = 0.9$.
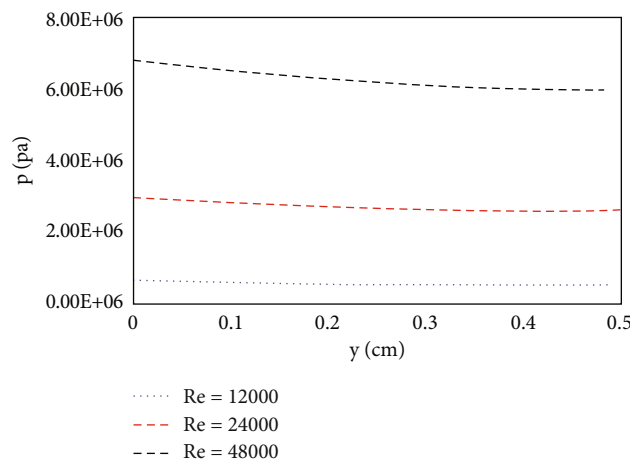

Figure 11: Pressure distribution for different Reynolds numbers on the vertical line at $\kappa = 0.2$ and $\varepsilon = 0.9$.

nearly constant, but within it, it increases from zero on the solid wall to the ultimate value at the boundary layer's border. The flow simulation is discussed in the following at a rotational Reynolds number of 12000. The velocity distributions at this Reynolds number are presented in Figure 10 in terms of streamlines and pressure contours. The formation of different vortices can be observed in these conditions. High-pressure and low-pressure zones on the cylinder are also identified. High-pressure regions occur between 270 and 360 degrees, and low-pressure areas are visible in the
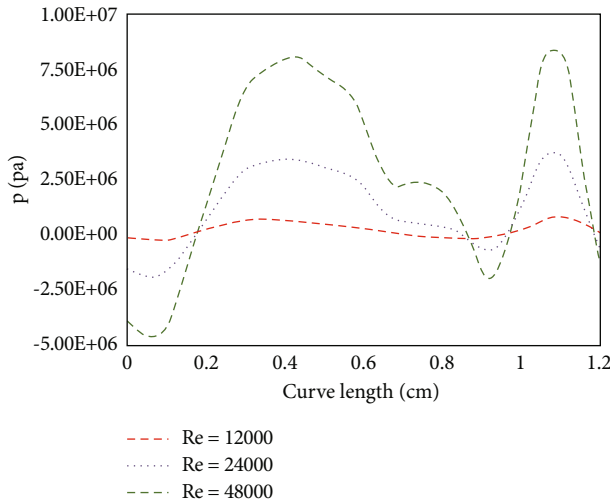
FIGURE 12: Pressure distribution around the cylinder for different Reynolds numbers on the vertical line at $\kappa = 0.2$ and $\varepsilon = 0.9$.

range of zero to 90 degrees and 180 to 270 degrees. The pressure changes between the two cylinders are also shown in Figure 11 at different Reynolds numbers.

The pressure distribution at the upper cross section of the inner cylinder on the vertical line increases with increasing Reynolds numbers, which is the process of pressure change toward the outer cylinder decreasing. The pressure distribution over the cylinder is also shown in Figure 12 at different Reynolds numbers.

It is seen from the pressure distribution figures, the pressure is experiencing complex changes at high Reynolds numbers. Therefore, the pressure diagram has multiple maximums and minimums at high Reynolds numbers. The difference between the maximum and minimum pressure around the cylinder increases with the increasing Reynolds number.

5. Conclusion

A characteristic-based scheme investigated the flow between two decentered cylinders in two different regimes. The parameters such as the Taylor number, eccentricity distance, Reynolds number, and radius ratio were considered the controlling fluid flow parameters between the cylinders. The inner cylinder was rotated counterclockwise while the outer cylinder was remained fixed. The major findings of the present study are outlined below:

(i) The asymmetric centrifugal forces produce Taylor vortices to the right of the internal rotating cylinder as the eccentricity grows at a constant Taylor number. As a result, this vortex is stretched at larger radius ratios and inclines leftward. The vortex stretching phenomena are dominated by Re and eccentricity

(ii) Taylor vortices do not appear for axial flow with no cylindrical rotation

(iii) Depending on the strength of Taylor vortices, the pressure oscillations could be fortified or dampened. As the eccentricity increases, the shear stress fluctuates, causing the pressure to rise

(iv) At different Taylor numbers in the narrowing part of the bearing, the pressure is greater than the wider part of the bearing, which is shaped by wedge forces pumped by the viscous forces

(v) The amount of shear stress and its variation on the cylinder, as well as the pressure on the cylinder, increases with increasing eccentricity

Data Availability

No data were used to support this study.

Conflicts of Interest

The authors declare that they have no conflicts of interest.

References

[1] A. A. Al-Rashed, A. Shahsavar, S. Entezari, M. Moghimi, S. A. Adio, and T. K. Nguyen, "Numerical investigation of non-Newtonian water-CMC/CuO nanofluid flow in an offset strip-fin microchannel heat sink: thermal performance and thermodynamic considerations," *Applied Thermal Engineering*, vol. 155, pp. 247–258, 2019.

[2] A. Dogonchi, A. J. Chamkha, and D. Ganji, "A numerical investigation of magneto-hydrodynamic natural convection of Cu–water nanofluid in a wavy cavity using CVFEM," *Journal of Thermal Analysis and Calorimetry*, vol. 135, no. 4, pp. 2599–2611, 2019.

[3] D. S. K. Reddy, P. Kumar, J. Makhija, A. A. Pasha, and A. Z. Hameed, "CFD of flow dynamic and heat transfer characteristics of dual step cylinders at Re = 2100," *Arabian Journal for Science and Engineering*, vol. 46, no. 12, pp. 12667–12683, 2021.

[4] Y.-J. Kim and Y.-K. Hwang, "Experimental study on the vortex flow in a concentric annulus with a rotating inner cylinder," *KSME international journal*, vol. 17, no. 4, pp. 562–570, 2003.

[5] G. Ma, C. Wu, and P. Zhou, "Wall slip and hydrodynamics of two-dimensional journal bearing," *Tribology International*, vol. 40, no. 7, pp. 1056–1066, 2007.

[6] S. Hamzehlouia and K. Behdinan, "A study of lubricant inertia effects for squeeze film dampers incorporated into high-speed turbomachinery," *Lubricants*, vol. 5, no. 4, p. 43, 2017.

[7] J. Frêne, M. Arghir, and V. Constantinescu, "Combined thin-film and Navier-Stokes analysis in high Reynolds number lubrication," *Tribology International*, vol. 39, no. 8, pp. 734–747, 2006.

[8] U. Singh, L. Roy, and M. Sahu, "Steady-state thermo-hydrodynamic analysis of cylindrical fluid film journal bearing with an axial groove," *Tribology International*, vol. 41, no. 12, pp. 1135–1144, 2008.

[9] M. M. Bhatti, L. Phali, and C. M. Khalique, "Heat transfer effects on electro-magnetohydrodynamic Carreau fluid flow between two micro-parallel plates with Darcy–Brinkman–Forchheimer medium," *Archive of Applied Mechanics*, vol. 91, no. 4, pp. 1683–1695, 2021.

[10] A. Shahid, M. M. Bhatti, R. Ellahi, and K. S. Mekheimer, "Numerical experiment to examine activation energy and bi-convection Carreau nanofluid flow on an upper paraboloid porous surface: application in solar energy," *Sustainable Energy Technologies and Assessments*, vol. 52, p. 102029, 2022.

[11] M. M. Bhatti, M. B. Arain, A. Zeeshan, R. Ellahi, and M. H. Doranehgard, "Swimming of gyrotactic microorganism in MHD Williamson nanofluid flow between rotating circular plates embedded in porous medium: application of thermal energy storage," *Journal of Energy Storage*, vol. 45, p. 103511, 2022.

[12] L. Roy and S. Laha, "Steady state and dynamic characteristics of axial grooved journal bearings," *Tribology International*, vol. 42, no. 5, pp. 754–761, 2009.

[13] D. Kumar, K. Ramesh, and S. Chandok, "Effectiveness of magnetic field on the flow of Jeffrey fluid in an annulus with rotating concentric cylinders," *Journal of the Brazilian Society of Mechanical Sciences and Engineering*, vol. 40, no. 6, p. 305, 2018.

[14] I. G. Currie, *Fundamental Mechanics of Fluids*, CRC Press, Taylor & Francis Group, 2013.

[15] M. Escudier, I. Gouldson, P. Oliveira, and F. Pinho, "Effects of inner cylinder rotation on laminar flow of a Newtonian fluid through an eccentric annulus," *International Journal of Heat and Fluid Flow*, vol. 21, no. 1, pp. 92–103, 2000.